

## Article

# The Influence of Multi-Size Basalt Fiber on Cemented Paste Backfill Mechanical Properties and Meso-Structure Characteristics

Xi Chen <sup>1,2</sup>, Huazhe Jiao <sup>1,2,\*</sup> , Juanhong Liu <sup>3</sup>, Yixuan Yang <sup>1,4,\*</sup>, Xinming Chen <sup>1,2</sup>, Liuhua Yang <sup>1,2</sup> , Wenxiang Zhang <sup>1,2</sup> and Tongyi Yang <sup>4</sup>

<sup>1</sup> School of Civil Engineering, Henan Polytechnic University, Jiaozuo 454003, China; 212108020053@home.hpu.edu.cn (X.C.); chenxinming@163.com (X.C.); yanglh2005@163.com (L.Y.); wenxiangz1998@163.com (W.Z.)

<sup>2</sup> State Collaborative Innovation Center of Coal Work Safety and Clean-Efficiency Utilization, School of Civil Engineering, Henan Polytechnic University, Jiaozuo 454003, China

<sup>3</sup> School of Civil and Resources Engineering, University of Science and Technology Beijing, Beijing 100083, China; juanhong1966@hotmail.com

<sup>4</sup> School of Environmental and Chemical Engineering, Jiangsu University of Science and Technology, Zhenjiang 212003, China; tongyi@just.edu.cn

\* Correspondence: jiaohuazhe@hpu.edu.cn (H.J.); yangyixuan@hpu.edu.cn (Y.Y.)

**Abstract:** As the mine enters the deep mining stage, there is a need to enhance the compressive strength and toughness of the backfill. The objective of this study is to examine the mechanical properties of cemented tailings backfill after the incorporation of multi-size fibers and to validate the toughening mechanism of basalt fibers (BFs). To achieve this, a series of basic mechanical property tests for multi-size BFs mixing were devised, accompanied by industrial computerized tomography (CT) scanning and discrete element simulation. This study shows that the compressive strength increases and then decreases with the increase of BF dosage at a certain percentage of each size, and the splitting tensile strength gradually increases with the increase of BF dosage. The compressive strength tends to decrease and then increase, and the splitting tensile strength increases and then decreases as the fiber size ratio changes. The distribution of cemented tailings backfill and BF within the discrete element model is random. A few BF cannot play a bridging role; however, a moderate amount of BF is relatively uniformly distributed in the model to form a network structure, which generates a bond between the particles and the matrix and can effectively limit the expansion path of cracks and enhance the toughness.

**Keywords:** cemented tailings backfill; CT scanning; microscopic pore structure; fiber orientation distribution; discrete element simulation



**Citation:** Chen, X.; Jiao, H.; Liu, J.; Yang, Y.; Chen, X.; Yang, L.; Zhang, W.; Yang, T. The Influence of Multi-Size Basalt Fiber on Cemented Paste Backfill Mechanical Properties and Meso-Structure Characteristics. *Minerals* **2023**, *13*, 1215. <https://doi.org/10.3390/min13091215>

Academic Editors: Abbas Taheri, Haiqiang Jiang, Liang Cui, Nan Zhou and Xiwei Zhang

Received: 27 June 2023

Revised: 13 September 2023

Accepted: 13 September 2023

Published: 15 September 2023



**Copyright:** © 2023 by the authors. Licensee MDPI, Basel, Switzerland. This article is an open access article distributed under the terms and conditions of the Creative Commons Attribution (CC BY) license (<https://creativecommons.org/licenses/by/4.0/>).

## 1. Introduction

Mining is a cornerstone industry of the national economy, providing 90% of China's energy and raw materials [1,2]. The development of mineral resources at the same time was accompanied by the generation of a large number of tailings [3]. A significant accumulation of stockpiled tailings occupies valuable land resources, resulting not only in pollution of the surrounding surface environment [4], but also posing risks of landslides, dam failures, and other accidents [5,6]. Furthermore, prolonged and intensive mining of mineral resources has led to the creation of voids within the layers of the underground ore body, resulting in the formation of mined-out areas. The existence of mined-out areas makes the safe production of mines face great safety problems [7]. Mined-out areas and tailing ponds have become important problems restricting the development of mines [8], and the development of resources and the protection of the environment have become a development paradox.

Paste-filling materials consist of components such as binders, aggregates, and chemical additives [9]. As a form of environmentally friendly tailings treatment [10], the paste filling mining method [11] transforms tailings of various particle sizes (unclassified tailings) into a toothpaste-like, non-segregating paste slurry for stockpiling and filling. This method effectively mitigates adverse factors such as surface subsidence and perimeter rock instability caused by mined-out areas [12]. Simultaneously, it enhances resource recovery rates, reduces environmental and safety hazards posed by mine waste, eases the strain on existing tailings dams, and achieves the “one waste to cure two hazards” principle [13].

With the depletion of shallow resources in China, deep resource extraction has become the future [14]. In the face of more complex underground environments, the filling material must enhance its strength to manage the intricate stress challenges encountered in deep mining, encompassing both static and dynamic loads [15,16]. The filling material inherently possesses weaknesses such as low strength and susceptibility to failure [17]. In complex environments, when the structural integrity of the filling material is compromised, internal cracks can rapidly expand and extend, leading to swift deterioration. As a consequence, the strength of the filling material fails to meet the demands of quarry filling. Presently, enhancing the strength of filler materials has emerged as a prominent research focus within both academic and industrial circles [18–20].

Research has demonstrated that the incorporation of fibers [21,22] into the filling process can effectively retard the degradation of the filling material [23,24]. Moreover, the bridging effect of fibers within the filling material [25–27] significantly enhances the mechanical properties of the cemented filling [28,29]. Following laboratory tests, Li [30] concluded that the unconfined compressive strength of fiber-reinforced cemented tailings backfill (FRCTB) increased with the increase in polypropylene (PP) fiber dosage, and the peak strain also increased from 0.39% to 1.45%. These findings indicate that the fibers effectively assume a bridging role during the failure of the tailings filling material. Xue [31] studied FRCTB using acoustic emission technology and an electronic universal testing machine and concluded that when the fiber dosage was 0.6% and the fiber length was 12 mm, the fiber exhibited the best enhancement performance. Xu [32] analyzed the backfill performance of fiber-reinforced cemented tailings at the microstructure level. The study revealed that fibers can retard crack propagation and constrain deformation, thereby enhancing structural strength and shifting the sample’s failure mode from brittleness to toughness.

The distribution of fibers in the internal structure of the filler has been studied in detail using many methods [33,34]. From a microscopic perspective [35,36], fibers enhance the internal structural density of the filling material [37] by occupying pores and retarding crack propagation, thereby bolstering the filling material’s strength [38–40]. Xue [41] carried out microscopic experiments on the fiber-reinforced coarse aggregate cement backfill. The study revealed that the addition of polypropylene fiber (PPF) resulted in a backfill that exhibited cracking resistance. An increase in the compactness of the interface transition zone and a reduction in pores were observed. Chen [42] performed scanning electron microscope (SEM) and nuclear magnetic resonance (NMR) microscopic tests, confirming that high-tensile-strength PP fibers enhance the tensile strength and ductility of the filling material while decreasing specimen porosity. The study concludes that the fibers can effectively integrate with cementitious materials, and the residual strength remains intact even after specimen fracture. Cao [43] studied cement-fiber-tailing matrix composites (CFMC) using industrial CT scanning and SEM. The addition of fiber dosage can effectively improve the compressive strength and toughness of tailings backfill specimens. From a microscopic perspective, the internal structure exhibits a marked reduction in pores, decreased interconnections, and increased particle packing density.

The previous research results are fruitful and representative. However, due to the similar densities of the fiber and the matrix, it is impossible to directly obtain a clear gray image of the internal structure when slicing, resulting in the inability to accurately identify the fiber in the three-dimensional reconstruction. This is the difficulty of realizing fiber

visualization. Therefore, the distribution of the internal structure of the filler material is still a challenging problem in microscopic research. This study designed a multi-scale basic mechanical performance test for (basalt fiber) BF mixing, obtained uniaxial compressive and flexural laboratory test results of tailings cemented filling, and studied the changes in mechanical properties under the influence of multi-scale. Industrial CT scanning technology is employed to construct an internal microstructure model and characterize fiber distribution. This information is then integrated with a discrete element program to analyze the distribution of microcracks in cemented tailings backfill, elucidating the reinforcing and toughening effects of BF on the backfill. A targeted study was conducted on the mechanical properties of mixed fibers in the filling body, obtaining the distribution of fiber structure inside the filling body, exploring the bridging effect of fibers in the filling body, and the toughening performance of the filling body. These findings serve to advance the application of fiber reinforcement technology in mining filling.

## 2. Materials and Methods

### 2.1. Materials

The unclassified tailing material used in the test was collected from a metal mine in Shandong Province, China, and its physical parameters are presented in Table 1. The chemical composition of the tailings sand significantly influences the quality of the filling material and the paste-filling process. Both its chemical composition and main mineral composition determine the suitability of this tailing sand for downhole filling. The tailing sand used in this test, along with its chemical composition, are presented in Table 2. Based on the tailing sand grain size test conducted using the Rise-2008 wet laser particle size meter, the grain size distribution curve of the tailing sand is depicted in Figure 1. The median particle size, D50, of the tailing sand, measures 51.2  $\mu\text{m}$ , categorizing it as fine tailing sand.

**Table 1.** Basic physical parameters of tailings.

Material	Proportion	Loose Bulk Density ( $\text{t}\cdot\text{m}^{-3}$ )	Specific Surface Area ( $\text{m}^2$ )	Dense Bulk Density ( $\text{t}\cdot\text{m}^{-3}$ )	Natural Repose Angle ( $^\circ$ )	Porosity (%)
Tailings	2.992	1.392	300–500	1.955	42.997	34.66

**Table 2.** Determination of chemical composition of tailings.

Mineral Constituent	Fe	SiO <sub>2</sub>	Al <sub>2</sub> O <sub>3</sub>	MgO	CaO	S	WO <sub>3</sub>	Misc.
Weight percentage (%)	9.41	47.62	5.26	2.87	11.56	2.21	0.04	21.03

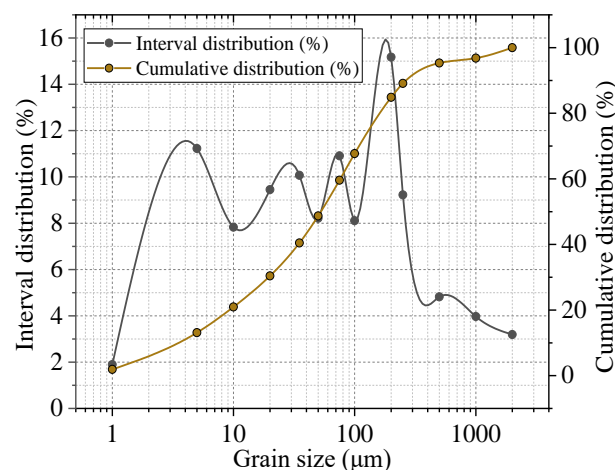


**Figure 1.** Particle size distribution of tailings.

A total of 42.5 R ordinary Portland cement is selected as a cementing agent, and its mineral compositions are CaO and SiO<sub>2</sub>. Laboratory water was utilized in the study. The density of basalt fibers is 2650 kg/m<sup>3</sup>. The elastic modulus is 100~110 GPa, and the tensile strength is 4150~4800 MPa. Three lengths of basalt fibers, 6 mm, 9 mm, and 12 mm, were selected for the experiment (Figure 2). The vinyl acetate-ethylene copolymer emulsion VAE emulsion was chosen in this study, with a solid content of 54.5%. The material is shown in Figure 3. The backfill specimen is depicted in Figure 4.

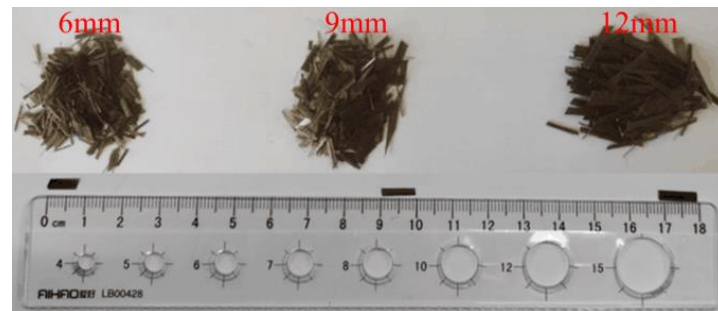


**Figure 2.** Basalt fiber.



**Figure 3.** Polymer Emulsion.



**Figure 4.** Cemented tailings backfill specimens.

## 2.2. Methods

The gray sand mass ratio is 1:8, and the selected slurry has a solid mass fraction of 68%. The sample mold used is a high-transparent acrylic pipe with an inner diameter of 50 mm and a wall thickness of 2 mm. This is the standard for testing the basic properties of construction mortar (JGJ/T 70-2009). The sample for testing is cured for 28 days under standard conditions: temperature ( $20 \pm 5$ ) °C and relative humidity ( $95 \pm 5$ )%. From the perspective of fiber length and fiber dosage, fiber mixing experiments with different sizes and lengths are designed. The materials utilized in this research include OPC, water, tailings, and basalt fiber. The experimental plan for this study is detailed in Table 3.

**Table 3.** Mixing ratio of filling materials (kg/m<sup>3</sup>).

Specimens		H1	H2	H3	H4	H5	H6	H7	H8	H9
OPC		110	110	110	110	110	110	110	110	110
Tailings		880	880	880	880	880	880	880	880	880
Water		466.6	466.6	466.6	467.3	467.3	467.3	468	468	468
Fiber dosage of each length	6 mm	0.5	0.5	1	1	1	2	1.5	1.5	3
	9 mm	0.5	0	0.5	1	0	1	1.5	0	1.5
	12 mm	0.5	1	0	1	2	0	1.5	3	0

Group H1 represents the incorporation of 6 mm fibers at 0.5 kg/m<sup>3</sup>, 9 mm fibers at 0.5 kg/m<sup>3</sup>, and 12 mm fibers at 0.5 kg/m<sup>3</sup>. Group H2 represents the incorporation of 6 mm fibers at 0.5 kg/m<sup>3</sup> and 12 mm fibers at 1 kg/m<sup>3</sup>. Group H3 represents the incorporation of 6 mm fibers at 1 kg/m<sup>3</sup> and 9 mm fibers at 0.5 kg/m<sup>3</sup>. Group H4 represents the incorporation of 6 mm fibers at 1 kg/m<sup>3</sup>, 9 mm fibers at 1 kg/m<sup>3</sup>, and 12 mm fibers at 1 kg/m<sup>3</sup>. Group H5 represents the incorporation of 6 mm fibers at 1 kg/m<sup>3</sup> and 12 mm fibers at 2 kg/m<sup>3</sup>. Group H6 represents the incorporation of 6 mm fibers at 2 kg/m<sup>3</sup> and 9 mm fibers at 1 kg/m<sup>3</sup>. Group H7 represents the incorporation of 6 mm fibers at 1.5 kg/m<sup>3</sup>, 9 mm fibers at 1.5 kg/m<sup>3</sup>, and 12 mm fibers at 1.5 kg/m<sup>3</sup>. Group H8 represents the incorporation of 6 mm fibers at 1.5 kg/m<sup>3</sup> and 12 mm fibers at 3 kg/m<sup>3</sup>. Group H9 represents the incorporation of 6 mm fibers at 3 kg/m<sup>3</sup> and 9 mm fibers at 1.5 kg/m<sup>3</sup>.

2.3. CT Scanning

The purpose of CT scanning is to pass X-rays through the sample using scanning equipment. As the X-rays penetrate the sample, their energy is attenuated, leading to changes. The detector captures these changes and converts them into signals. Subsequently, the X-rays, now transformed into digital signals, are transmitted to a computer system. After undergoing computer processing, these signals ultimately result in the formation of high-resolution digital images that reflect the material components of the sample. Owing to distinct density variations among tailing sand, cement, and initial defects, these three substances appear with varying levels of brightness in the image. Initial defects are depicted as black, while the higher-density tailing sand appears brighter, and the cement exhibits a shade between these two colors.

An industrial CT scanner (Figure 5) produced by General Electric Company (GE) in the United States was used to scan the filling specimen, a cylindrical specimen measuring 25 mm in diameter and 50 mm in height [44–46]. The sample scanning accuracy used in this experiment reached 35.71 μm. The size of the studied sample is relatively large; therefore, a micro-focus X-ray source is used to achieve a high scanning-resolution instrument loading system. The maximum voltage of the micro-focus X-ray source is 240 kV, and the maximum power is 320 W. The maximum axial pressure in the loading system of the equipment is 100 kN, the maximum confining pressure is 30 MPa, the maximum axial displacement is 20 mm, and the axial displacement rate is 0.01~3 mm·min<sup>-1</sup>.

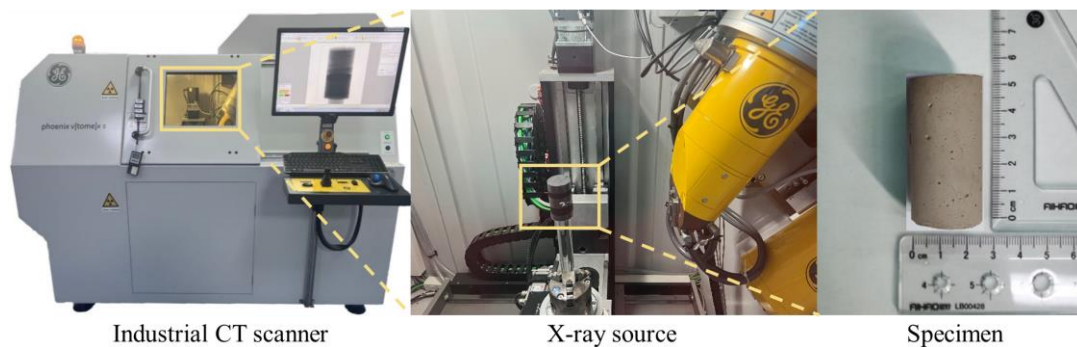


**Figure 5.** Scanning specimen and placement.

### 3. Theory

#### 3.1. Fiber Search Cone

When tracing and reconstructing BF in the microscopic model, the cylinder correlation method needs to be used to set the fiber segmentation tracking correlation coefficient. Based on the search cone algorithm (Figure 6), set the length, angle, and minimum step size parameters to be segmented and tracked [47,48]. The search cone will determine the voxel  $P$  with the highest correlation coefficient as the starting point for fiber tracking, and the voxel placement angle is  $\gamma$ .  $P_c$  is another related voxel within the search cone, connecting  $P$  and  $P_c$  voxels to form fiber segments, and  $P_c$  is a fiber composed of multiple fiber segments that are the same as  $PP_c$ . The length, tolerance radius, and outer diameter of the cylindrical model (as the inner diameter is selected as 0 in this model, the outer diameter and radius) are presented, along with a schematic diagram of the fiber tracking model parameters and algorithm.

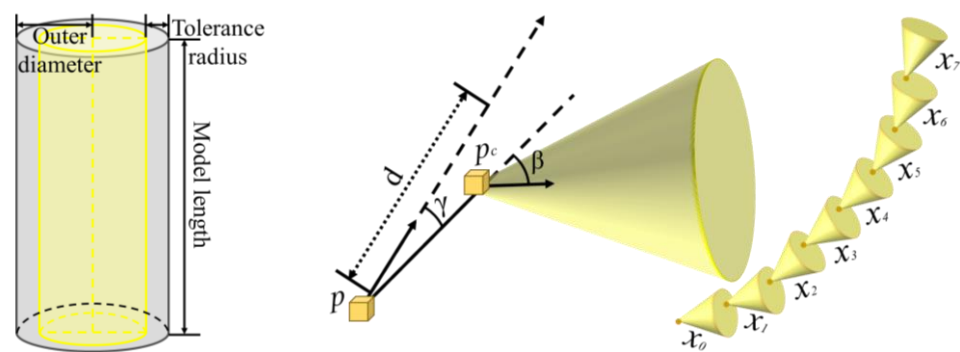


**Figure 6.** Search cone tracking schematic diagram (where,  $d$  is the distance,  $P$  and  $P_c$  are the starting points of pixels,  $\gamma$ ,  $\beta$  is the search angle, and  $X_0, X_1, X_2, X_3, X_4, X_5, X_6$  and  $X_7$  are the fiber search cones).

Based on the search cone algorithm shown in Figure 6, after determining the starting point of fiber tracking, connecting through the individual tracking points will result in the formation of fiber segments, which in turn will compose the fibers. The results obtained via this method are able to reconstruct the fibers inside the filling body.

#### 3.2. Fiber Distribution Angle

The reconstructed BF three-dimensional angle distribution is not applicable to PFC 2D [49]. Therefore, it is considered to convert the 3D angle of BF into a planar angle and apply it to the construction of a discrete element model [50–52]. As shown in Figure 7, the conversion formula between the two is:

$$\epsilon = \arctan\left(\frac{\cos \theta \sin \varphi}{\sin \theta}\right) \tag{1}$$

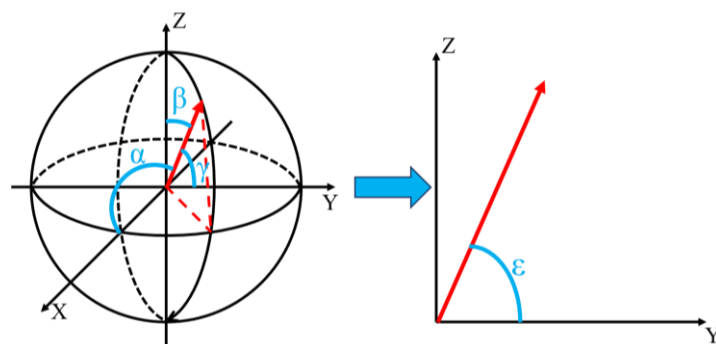


**Figure 7.** Conversion from three-dimensional angle to plane angle (where,  $\alpha$ ,  $\gamma$ ,  $\beta$  and  $\epsilon$  is the angle).

In the reconstructed BF distribution model, the angles are presented in spherical coordinates. In order to facilitate the application of fiber distribution angles in subsequent discrete element models, it is necessary to convert spherical coordinates into Cartesian coordinate systems for a reasonable selection of plane angles. The coordinate conversion formula for two coordinate systems is as follows:

$$\alpha = \arccos(\sin \theta \cos \varphi) \quad (2)$$

$$\beta = \arccos(\sin \varphi \cos \theta) \quad (3)$$

$$\gamma = \beta \quad (4)$$

where,  $\theta$  is the polar angle in the spherical coordinate system, i.e., the angle between the fiber length and the Z-axis,  $0^\circ < \theta < 90^\circ$ ;  $\varphi$  is the azimuth angle in the spherical coordinate system, i.e., the angle between the projection of the fibers on the XY axis plane and the X axis,  $0^\circ < \varphi < 360^\circ$ ;  $\alpha$  is the angle between BF and the X-axis in the Cartesian coordinate system;  $\beta$  is the angle between BF and the Y-axis in the Cartesian coordinate system;  $\gamma$  is the angle between BF and the Z-axis in the Cartesian coordinate system.

By applying the aforementioned formula to convert spherical coordinates into Cartesian coordinates, a quantitative analysis of fiber orientation within the CT scan-reconstructed filling material can be conducted. This analysis yields the distribution angles of the fibers. Defining the ratio of the number of BFs to the total number of BFs within a specified angle range as the relative frequency.

### 3.3. Force Displacement Law

As a particle flow program, PFC mainly uses the discrete element method to simulate the interaction and movement of particles or particle aggregates [53,54]. The calculation principle is mainly based on Newton's second law and the force-displacement law, where the force-displacement law acts on the contact point between particles and between particles and walls. Through the contact point, the relative displacement and contact force of two contact particles are connected. If the contact point is between two particles, the normal direction of the contact plane is the direction of the line connecting the centers of the two particles, as shown in Figure 8. If it is the contact between particles and the wall, the normal direction is the shortest straight line from the particle center to the wall, as shown in Figure 9.

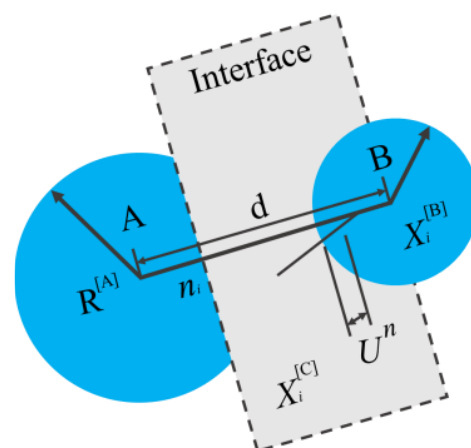
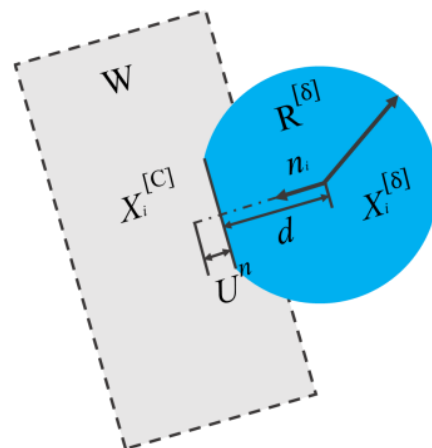


Figure 8. Contact between particles.



**Figure 9.** Contact between particles and wall (where,  $d$  refers to the distance,  $W$  refers to the contact surface,  $U^n$  refers to the overlap between particles, A, B refers to particles A and B, and  $X_i^{[C]}$  refers to the position of the contact point between particles).

The calculation formula for the normal vector  $n_i$  of the contact plane between two particles and the distance  $d$  between the two ball centers in Figure 8 is as follows:

$$n_i = \frac{x_i^{[B]} - x_i^{[A]}}{d} \quad (5)$$

$$d = |x_i^{[B]} - x_i^{[A]}| = \sqrt{(x_i^{[B]} - x_i^{[A]})(x_i^{[B]} - x_i^{[A]})} \quad (6)$$

The formula for calculating the overlap amount  $U^n$  between particles is shown in Equation (7):

$$U^n = \begin{cases} R^{[A]} + R^{[B]} - d \\ R^{[\delta]} - d \end{cases} \quad (7)$$

where,  $R^{[A]}$  is the radius of particle A;  $R^{[B]}$  is the radius of particle B;  $R^{[\delta]}$  is the radius of particle  $\delta$ .

The simulation parameters governing interactions between particles, as obtained from the equations mentioned above, are derived by simulating particle interactions and motions, either individually or within assemblies. These parameters serve as the foundation for generating the structural model of the filling material. Subsequently, this model is imported into the PFC software for discrete element simulation.

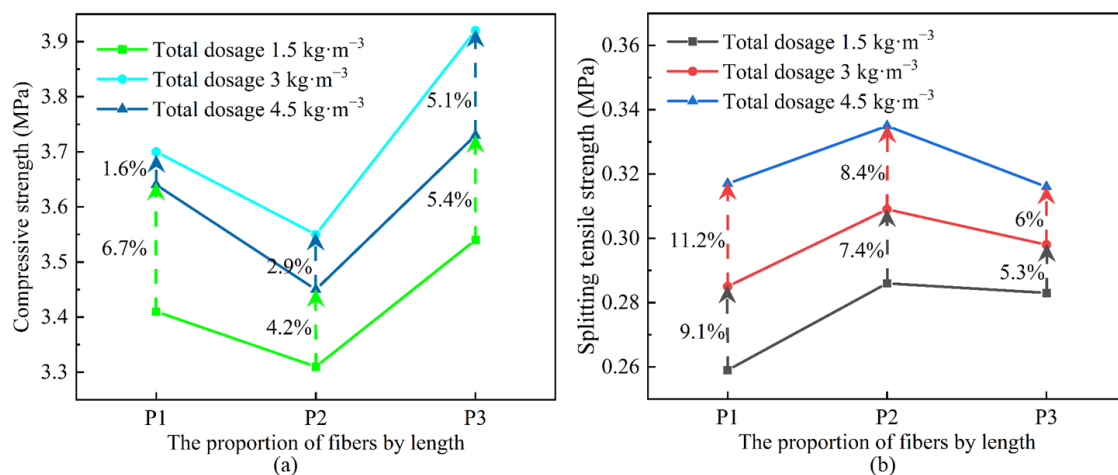
## 4. Results and Discussion

### 4.1. Mechanical Performance Test

The influence of different lengths of BF on the filling body varies, and longer BF tends to form a surrounding state. Under the same dosage, the number of effective fibers per unit area decreases and the connection effect weakens. However, shorter BF is easily pulled out due to the tensile effect of the filling material cracking, and it cannot exert its function. Therefore, the research analysis only considers the interaction between three different sizes of BF with fiber lengths of 6 mm, 9 mm, and 12 mm and conducts uniaxial compression and splitting tensile tests. Based on the test results, the influence of multi-scale BF mixing conditions on the mechanical properties of the filling body is analyzed. The measured strength results are shown in Table 4 and Figure 10.

**Table 4.** Mechanical properties test of filling under multi-scale BF mixing.

Specimen	BF Dosage ( $\text{kg}\cdot\text{m}^{-3}$ )			Compressive Strength (MPa)	Splitting Tensile Strength (MPa)
	6 mm	9 mm	12 mm		
H1	0.5	0.5	0.5	3.41	0.259
H2	0.5	0	1	3.31	0.286
H3	1	0.5	0	3.54	0.283
H4	1	1	1	3.70	0.285
H5	1	0	2	3.55	0.309
H6	2	1	0	3.92	0.298
H7	1.5	1.5	1.5	3.64	0.317
H8	1.5	0	3	3.45	0.335
H9	3	1.5	0	3.73	0.316

**Figure 10.** The trend of mechanical strength changes under the conditions of multi-scale BF mixing ((a) Compressive Strength; (b) Splitting Tensile Strength).

P1, P2, and P3 represent the proportion of BF content in each length (6 mm:9 mm:12 mm), which is 1:1:1, 1:0:2, and 2:1:0 in sequence. We conducted uniaxial compressive tests on samples mixed with multiple sizes of BF, and the compressive strength results of the filling body are shown in the Figure 10. With the increase in BF dosage, the uniaxial compressive strength of the filling body shows a trend of first increasing and then decreasing. The optimal BF dosage is  $3.0 \text{ kg}\cdot\text{m}^{-3}$ , which increases the compressive strength by 10.7% compared to the other two BF dosage groups, and the other two groups increase by 8.5% and 7.2%, respectively. Analysis shows that under the condition of constant total dosage, the compressive strength of the filling decreases when the proportion of BF of 12 mm increases.

The splitting tensile test results of the filling body under the condition of multi-scale BF mixing are shown in Table 3. Overall, the splitting tensile strength increases with the increase in BF content. When the proportion of BF content in each length is 1:1:1, the splitting tensile strength is the highest. When the BF content increases from  $1.5 \text{ kg}\cdot\text{m}^{-3}$  to  $3 \text{ kg}\cdot\text{m}^{-3}$ , the tensile strength increases by 9.1%. When the BF content is  $4.5 \text{ kg}\cdot\text{m}^{-3}$ , the tensile strength increases by 11.2% compared to  $3 \text{ kg}\cdot\text{m}^{-3}$ .

#### 4.2. Interaction Effects Analysis of Multi-Size Fibers

The multi-scale BF mixing experiment is based on the results of orthogonal experiments with a polymer dosage of 3%. The proportions of 6 mm, 9 mm, and 12 mm BF are adjusted while maintaining the total dosage of  $1.5 \text{ kg}\cdot\text{m}^{-3}$ ,  $3 \text{ kg}\cdot\text{m}^{-3}$ , and  $4.5 \text{ kg}\cdot\text{m}^{-3}$ . Therefore, the research analysis only considers the interaction between three different sizes of BF.

Due to the fact that when the total BF dosage is constant, the dosage of each length of BF is not uniform, it is not possible to study the effect of factor interaction from the perspective of BF length difference using SPSS. Therefore, we consider conducting a statistical analysis of variance results from the perspectives of total BF dosage (D) and the proportion of BF in each length (E). The analysis results are shown in Table 5.

**Table 5.** Statistical analysis results of bivariate factors.

Source of Variance *	Dependent Variable	$S_S$	$D_F$	$M_S$	$F$	$p$
Corrected model	Compressive strength	51.914	8	6.489	212.377	<0.001
	Splitting tensile strength	0.842	8	0.105	163.241	<0.001
Intercept	Compressive strength	23,062.361	1	23,062.361	754,768.164	<0.001
	Splitting tensile strength	160.205	1	160.205	248,593.966	<0.001
D	Compressive strength	27.681	2	13.841	452.964	<0.001
	Splitting tensile strength	0.657	2	0.328	509.690	<0.001
E	Compressive strength	22.964	2	11.482	375.782	<0.001
	Splitting tensile strength	0.143	2	0.072	111.207	<0.001
D × E	Compressive strength	1.269	4	0.317	10.382	0.002
	Splitting tensile strength	0.041	4	0.010	16.034	<0.001
Error	Compressive strength	0.275	9	0.031		
	Splitting tensile strength	0.006	9	0.001		
Total	Compressive strength	23,114.550	18			
	Splitting tensile strength	161.052	18			
Revised total	Compressive strength	52.189	17			
	Splitting tensile strength	0.847	17			

\*  $S_S$  is the sum of squares of variation.  $D_F$  is the degree of freedom.  $M_S$  is the variance. The size of the  $p$  represents significance.

The effects of single factor D, E response, and second-order interaction on each intensity are extremely significant ( $p < 0.01$ ). The strength analysis results under single factor response show that  $F_D > F_E$ , indicating that the total BF dosage has the greatest impact on strength among the two factors. Compared with the single-factor response results, the second-order interaction results showed  $F_D > F_E > F_{D \times E}$  for compressive and splitting tensile strength, indicating that the first-order interaction had a secondary impact on compressive and splitting tensile strength.

The trend of changes in flexural strength under the interaction of three lengths of BF shows that the interaction between 6 mm and 12 mm BF is more significant. When the dosage of 6 mm BF remains unchanged, the flexural strength increases with the increase in 12 mm BF dosage. When the dosage of 12 mm BF remains unchanged, the flexural strength increases with the increase in 6 mm BF dosage. When the content of 9 mm length BF remains unchanged, the flexural strength increases with the increase in 12 mm length BF content. However, when the content of 12 mm length BF remains unchanged, the flexural strength increases with the increase in 9 mm length BF content.

Based on the test results of the mechanical properties of a multi-size BF mixture, the effects of various strength distributions are compared and analyzed. Since the BF content is the main influencing factor of mechanical properties, and considering that the polymer content is set at 3% in the multi-size BF mixing test, after comprehensive analysis, single-mixed and mixed samples with 3% of the polymer content,  $1.5 \text{ kg} \cdot \text{m}^{-3}$ ,  $3.0 \text{ kg} \cdot \text{m}^{-3}$  and  $4.5 \text{ kg} \cdot \text{m}^{-3}$  of fiber content are selected for strength distribution comparative analysis, as shown in Figure 9. The filling body under the condition of multi-scale BF mixing has significant advantages in improving compressive strength; however, the improvement effect in splitting tensile strength is not significant.

The trends in the compressive strength of the filler for the interaction of the three sizes of BF are shown in Figure 11. The interaction between 6 mm and 9 mm has a significant impact on compressive strength. The dosage of BF with a length of 6 mm remains unchanged, while the dosage of BF with a length of 9 mm increases. The compressive strength first increases and then decreases. When the dosage of BF with a length of 9 mm remains unchanged, the compressive strength also shows the same trend as when the dosage of BF with a length of 6 mm increases. Under the interaction of 12 mm, 6 mm, and 9 mm lengths of BF, the compressive strength decreases with an increase in the addition of 6 mm and 9 mm lengths of BF, while the amount of BF remains unchanged.

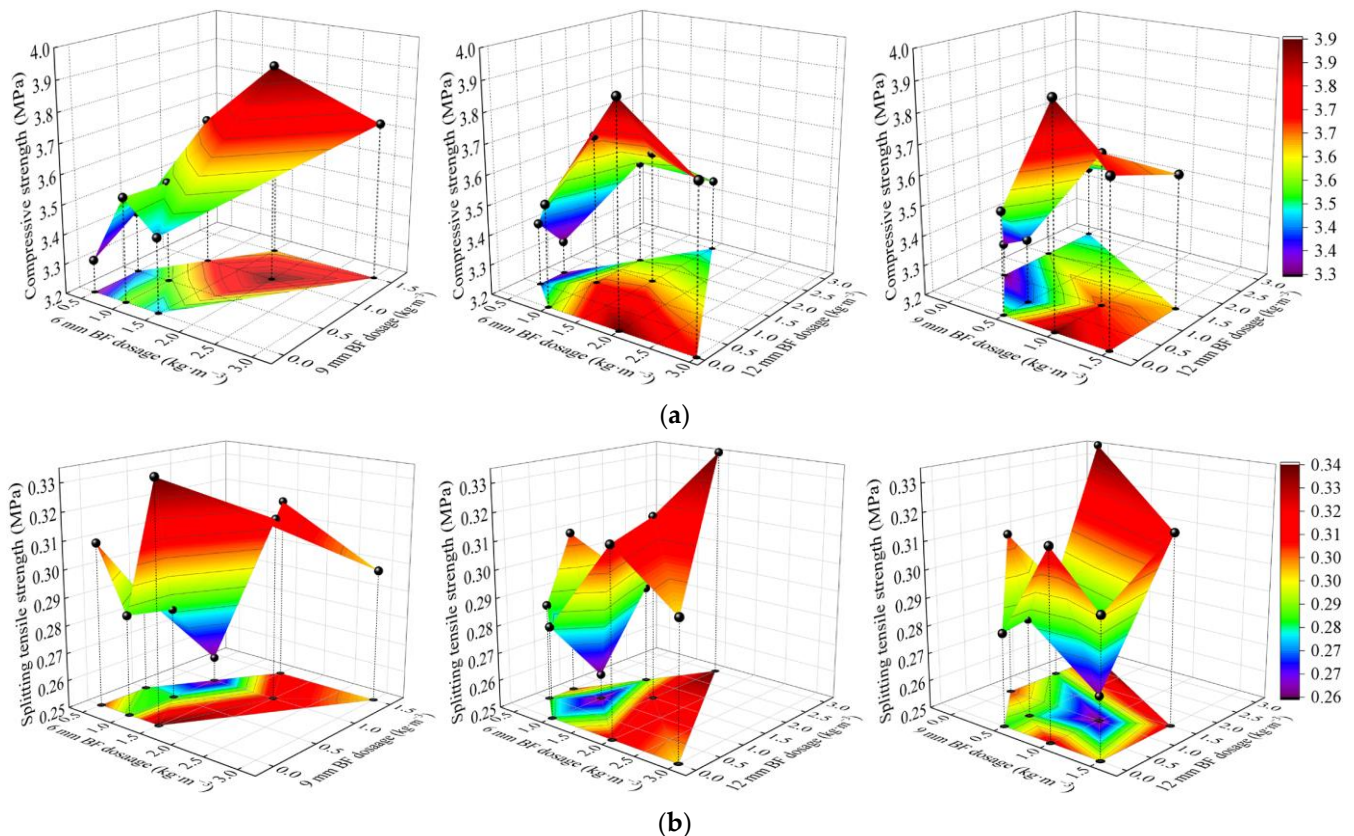


**Figure 11.** Influence of the interaction of 6 mm, 9 mm, and 12 mm BF on mechanical strength: (a) Trend of compressive strength changes under the interaction of multi-scale BF; (b) Trend of splitting tensile strength under the interaction of multi-scale BF.

It can be seen that the interaction between 6 mm and 12 mm BF is significant for the splitting tensile strength of the filling. When the content of 6 mm BF remains unchanged, the splitting tensile strength increases with the increase in 12 mm BF content. However, when the content of 12 mm BF remains unchanged, the splitting tensile strength first increases and then decreases with the increase in 6 mm BF content, indicating that the high content of long BF effectively improves the splitting tensile strength of the filling body. It shows the same trend of change in splitting tensile strength. When the content of 9 mm-long BF remains unchanged, the splitting tensile strength increases with the increase in 12 mm-long BF content. However, when the content of 12 mm-long BF remains unchanged, the splitting tensile strength first increases and then decreases with the increase in 9 mm-long BF content.

#### 4.3. Backfill Mesoporous Structure

As the main defect inside the filling body, the distribution of pores in the filling body matrix has a significant impact on the mechanical properties of the filling body. Perform

threshold segmentation on CT scan images, extract pores from 2D slices, and reconstruct 3D pores through stacking of slices, as shown in Figure 12.

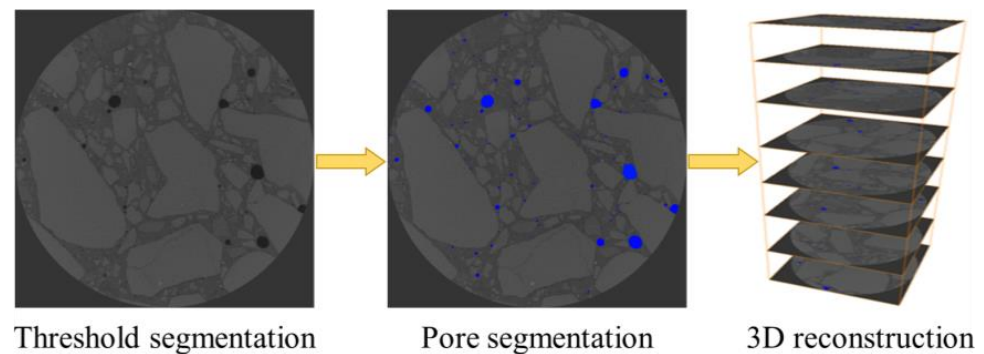


**Figure 12.** Pore extraction and reconstruction (where, blue is the marking and extraction of pores).

The scanning results of the H2, H5, and H8 groups of samples were processed, and the three-dimensional pore distribution characteristics inside each group of samples are shown in Figure 13. The porosity changes of the H2, H5, and H8 specimens under the condition of multi-scale fiber mixing are the same as those of the orthogonal experimental group. With the increase in fiber content, the porosity first decreases and then increases, showing a range of 35.9% and 22%, respectively.

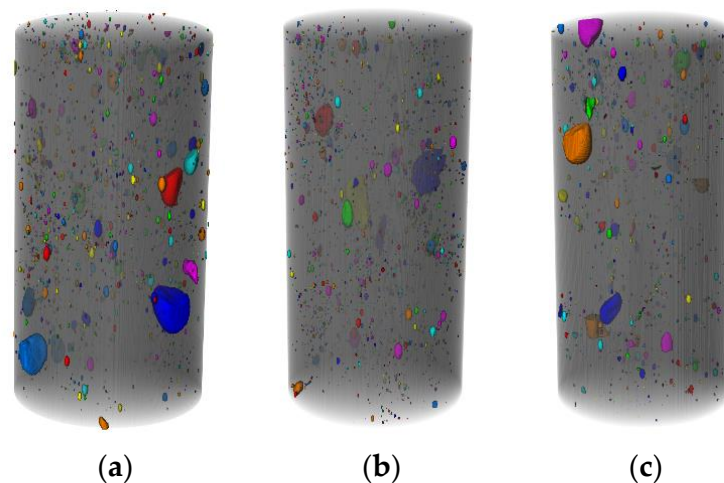


**Figure 13.** Meso-pore model of each group of specimens: (a) H2 group; (b) H5 group; (c) H8 group (where, the color represents the rendering effect of extracting pores in reconstruction).

As shown in Table 6, when the same fiber content is added, the porosity of the sample is relatively small and the number of pores is small; however, the average pore diameter is relatively large under the condition of multi-scale fiber mixing. Under the condition of multi-scale fiber mixing, the porosity of the H2, H5, and H8 samples decreased first and then increased with the increase in BF content, showing changes of 35.9% and 22%, respectively.

In the pore model, according to the equivalent diameter of pores, they can be divided into macropores, mesopores, and micropores. The equivalent diameter is greater than 1000  $\mu\text{m}$ , which is called a macropore. Pores with a diameter between 100  $\mu\text{m}$  and 1000  $\mu\text{m}$  are called mesopores, while pores with a diameter less than 100  $\mu\text{m}$  are called micropores, as shown in Figure 14. Figure 15 shows the proportion of the number of pore types within the sample.

**Table 6.** Pore information of each group of specimens.

Specimen		H2	H5	H8
Porosity		0.78%	0.50%	0.61%
Total number of pores		3442	3927	2585
Pore diameter (μm)	Average	191.8	158.7	182.2
	Minimum	48.1	46.6	46.4
	Maximum	4356.5	4195.5	4209.0
	Median	133.6	120.5	123.7
Pore area (μm <sup>2</sup> )	Average	$2.94 \times 10^5$	$2.08 \times 10^5$	$2.87 \times 10^5$
	Minimum	$4.63 \times 10^3$	$4.34 \times 10^3$	$4.30 \times 10^3$
	Maximum	$6.68 \times 10^7$	$7.84 \times 10^7$	$6.28 \times 10^7$
	Median	$5.66 \times 10^4$	$4.64 \times 10^4$	$4.72 \times 10^4$
Pore volume (μm <sup>3</sup> )	Average	$5.56 \times 10^7$	$3.14 \times 10^7$	$5.82 \times 10^7$
	Minimum	$5.81 \times 10^4$	$5.29 \times 10^4$	$5.23 \times 10^4$
	Maximum	$4.33 \times 10^{10}$	$3.87 \times 10^{10}$	$3.90 \times 10^{10}$
	Median	$1.12 \times 10^6$	$8.66 \times 10^5$	$9.78 \times 10^5$

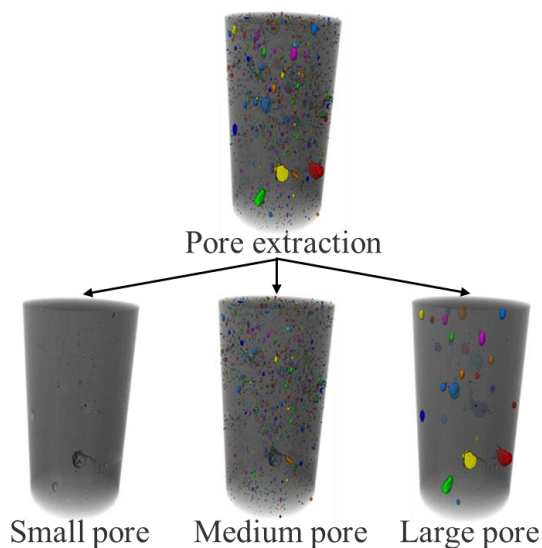


**Figure 14.** Pore classification.

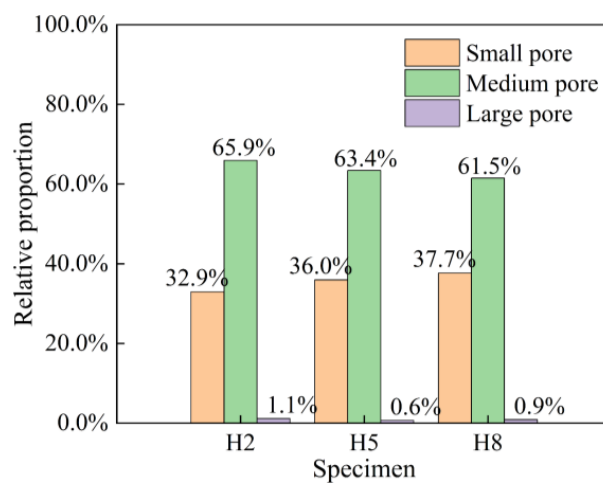


**Figure 15.** Proportion of pore types.

It can be seen that the pores of each sample are mainly composed of medium pores, followed by a proportion of small pores. The improvement effect of internal pores in the sample is more significant under the mixing of multi-scale BF. As the BF content increases, the proportion of pores in the filling body gradually decreases, the proportion of small pores gradually increases, and the proportion of large pores also shows a trend of first decreasing and then increasing. Comprehensive analysis shows that the best improvement effect of BF on the internal pore structure of the filling body is achieved during the mixing of multi-scale BF.

#### 4.4. Backfill Fiber Distribution

Due to the large size obtained from CT scanning, fiber tracking of the entire sample area requires too much memory and is not easy to calculate. Therefore, after considering the memory size and computing power of the computer, the cube area at the center of the sample was selected for fiber tracking reconstruction processing, as shown in Figure 16.

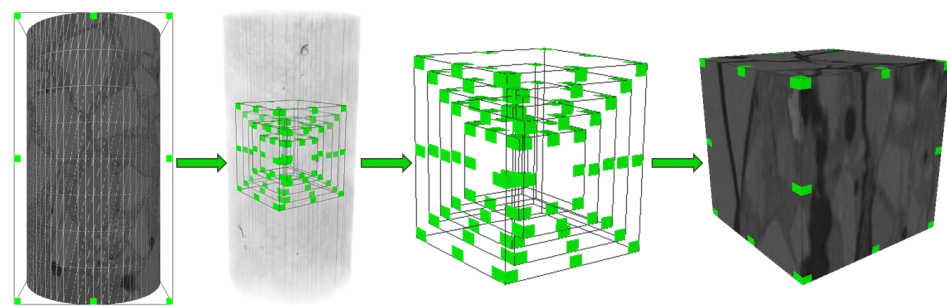


**Figure 16.** Selecting the REV.

In Figure 17, in the H2, H5, and H8 groups, the relative frequencies of BF and X-axis in the range of  $80^\circ\sim 90^\circ$  are the largest, which are 0.41, 0.38, and 0.3, respectively. Compared to the other two groups, the H2 group has a lead angle distribution ranging from  $40^\circ$  to  $90^\circ$ . The angles between the three groups and the Y-axis are relatively evenly distributed within  $0^\circ$  to  $90^\circ$ , and there are no significant features. The angle between BF and Z-axis in the H2, H5, and H8 groups is concentrated within  $30^\circ$  to  $90^\circ$ , while the BF distribution angle in the H2 group shows a gradually decreasing trend within  $30^\circ$  to  $90^\circ$ .

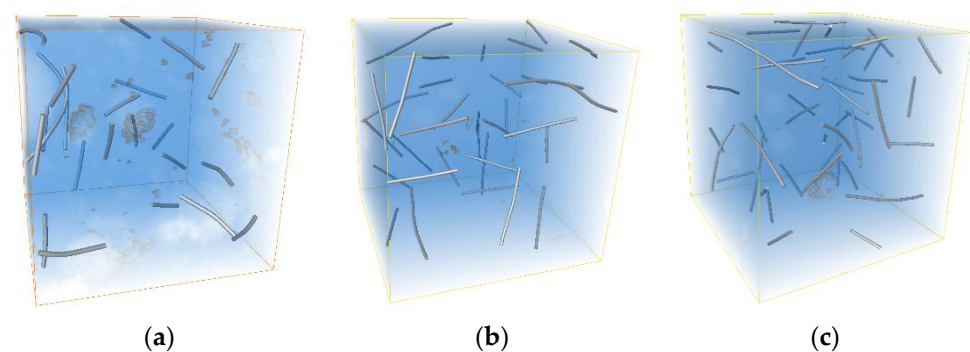


**Figure 17.** Fiber distribution model of each group of specimens: (a) H2 group; (b) H5 group; (c) H8 group.

Convert the three-dimensional Cartesian coordinate angle of BF into a two-dimensional plane angle, and the relative frequency of BF distribution under the plane angle in each group of samples is shown in Figure 18. The angle distribution range of BF in the H2 group sample mixed with multi-size BF is wider, and its main distribution range is  $40^\circ\sim 50^\circ$ ,  $80^\circ\sim 90^\circ$  and  $150^\circ\sim 180^\circ$ . When the BF content increases to  $3.0\text{ kg}\cdot\text{m}^{-3}$  and  $4.5\text{ kg}\cdot\text{m}^{-3}$ , the BF angle distribution range becomes more concentrated and tends in the horizontal direction. The distribution characteristics of BF in the H8 group are particularly significant,

and the relative frequencies of BF angle distribution at 10° and 180° reach 0.136 and 0.159, respectively.

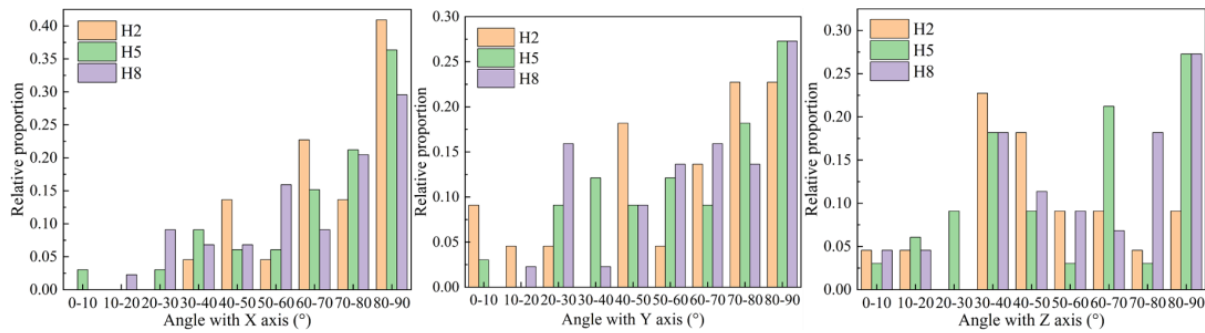


Figure 18. Histogram of BF Angle Distribution in Groups H2, H5, and H8.

4.5. Backfill Mesoscopic Discrete Element

In order to make the backfill compression test model fully correspond to the laboratory test process in the loading process, the calibration of the microscopic parameters of the backfill compression test model is completed by comparing the stress–strain curve of the numerical simulation process and the laboratory test. The calibration process is shown in Figure 19. By adjusting the values of pb\_emod, pb\_coh, and pb\_ten in the model micromechanical parameters to match the stress–strain curve of the laboratory test and simulation test, the final adjusted micromechanical parameters based on the curve calibration results in Figure 19 are shown in Table 7.

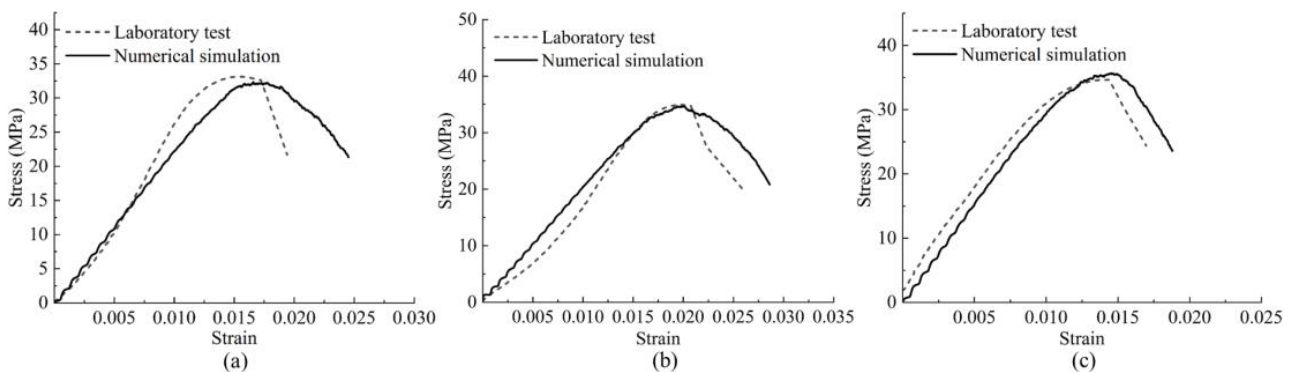


Figure 19. Calibration of stress-strain curve ((a) H2; (b) H5; (c) H8).

Table 7. Calibration results of meso-mechanical parameters of compression model.

Specimen	ball_emod = pb_emod	pb_coh	pb_ten			fric	pb_fa
			Ball-Ball	Ball-Pebble	Pebble-Pebble		
H2	$1.2 \times 10^9$	$1.1 \times 10^7$	$1.1 \times 10^7$	$7 \times 10^6$	$7 \times 10^6$	0.25	50
H5	$8 \times 10^8$	$9 \times 10^6$	$8 \times 10^6$	$5 \times 10^6$	$5 \times 10^6$		
H8	$1.3 \times 10^9$	$8 \times 10^6$	$7 \times 10^6$	$5 \times 10^6$	$5 \times 10^6$		

Due to the irregularity of the force-displacement curve obtained from the splitting tensile test simulation and the difficulty in matching the curve obtained from the laboratory test process, it was chosen to control the elastic modulus of the model by keeping the values of ball\_emod and pb\_emod unchanged on the basis of the microscopic parameters of the compressive test model. By adjusting the sizes of pb\_coh and pb\_ten, the loading force at the time of model failure was similar to that of the laboratory test. The final parameter calibration results are shown in Table 8.

**Table 8.** Calibration results of meso-mechanical parameters of splitting tensile model.

Specimen	ball_emod = pb_emod	pb_coh	pb_ten			fric	pb_fa
			Ball-Ball	Ball-Pebble	Pebble-Pebble		
H2	$1.2 \times 10^9$	$1 \times 10^6$	$5 \times 10^5$	$4 \times 10^5$	$4 \times 10^5$	0.25	50
H5	$8 \times 10^8$	$1 \times 10^6$	$8 \times 10^5$	$6 \times 10^5$	$6 \times 10^5$		
H8	$1.3 \times 10^9$	$1.2 \times 10^6$	$6 \times 10^5$	$4 \times 10^5$	$4 \times 10^5$		

The failure mode of the discrete element model of the filling body under parameter calibration is similar to the laboratory test results, indicating the feasibility of conducting a discrete element simulation of the filling body. As shown in Figure 20, the fracture characteristics of the compressive model in the multi-scale BF mixing test are shown in red lines. Moreover, the comparison of the damage situation of the laboratory test samples shows that there is a small difference between the damage characteristics of the discrete element model of the filling body and the laboratory test. The main reason for the analysis is the randomness of the distribution of coarse aggregate and BF within the sample. Due to the mixing of multi-scale BF, the H2, H5, and H8 models exhibit high residual strength in terms of failure. On the one hand, due to the randomness of the shape and distribution of aggregates within the model, there is no significant change in the failure patterns of each group of models. On the other hand, although the compressive failure characteristics of the numerical model are similar to those of laboratory experiments, the construction of the two-dimensional model cannot fully reflect the failure characteristics of backfill.

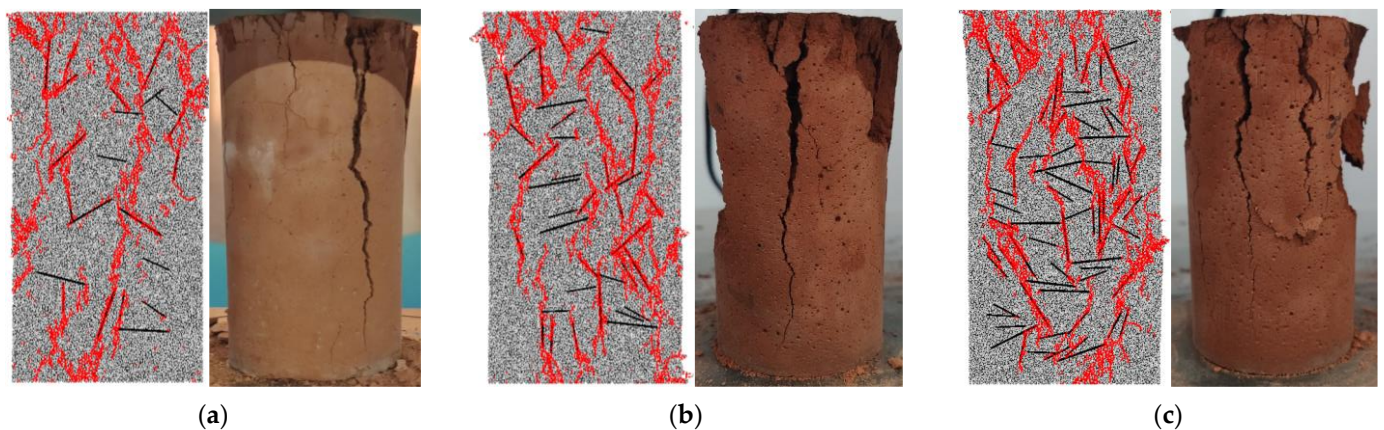


**Figure 20.** Comparison between compressive failure characteristics of backfill model and laboratory test results: (a) H2 group; (b) H5 group; (c) H8 group.

The data obtained in the discrete element simulation (Figure 21) show that the angle distribution range of BF of the H2 group sample mixed with multi-size BF is wider, and its main distribution range is  $40^\circ \sim 50^\circ$ ,  $80^\circ \sim 90^\circ$  and  $150^\circ \sim 180^\circ$ ; When the BF content increases to  $3.0 \text{ kg} \cdot \text{m}^{-3}$  and  $4.5 \text{ kg} \cdot \text{m}^{-3}$ , the BF angle distribution range becomes more concentrated and tends to the horizontal direction. The distribution characteristics of BF in the H8 group are particularly significant, and the relative frequencies of BF angle distribution at  $10^\circ$  and  $180^\circ$  reach 0.136 and 0.159, respectively. Overall, the orientation of BF in space is mostly close to the horizontal direction, and the conclusions obtained are consistent with those in the reconstruction model, confirming the feasibility of discrete element simulation of filling bodies.

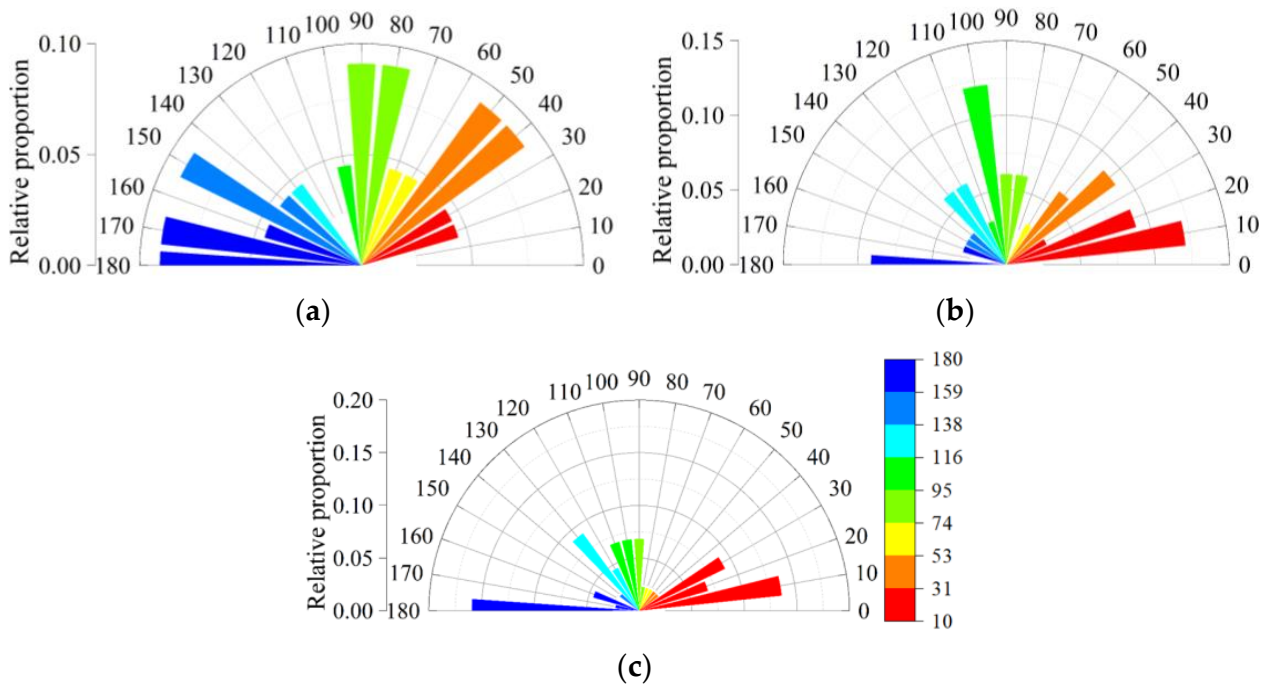


**Figure 21.** Plane angle distribution of BF: (a) H2 group; (b) H5 group; (c) H8 group.

## 5. Conclusions

To ensure the safety and efficiency of mine production, it is imperative to enhance the strength and quality of the filling material. For this purpose, research on the physical characteristics of the filling body is carried out, the internal fine structure of the filling body is observed by industrial computerized tomography scanning, and the destruction mode of the filling body is analyzed by discrete element simulation so as to improve the physical strength quality of the filling body. From the findings of this study, the following conclusions were drawn:

- (1) The mechanical property tests revealed that mixing various sizes of BFs effectively filled concrete pores, consequently enhancing both the compressive and split tensile strengths of the filled material. The tests showed the existence of an optimum fiber blend and an optimum fiber size ratio.
- (2) Analysis of the second-order interactions reveals a significant advantage of the filler in the multiscale BF mixing condition for enhancing compressive strength, although the enhancement in split tensile strength is not substantial.
- (3) Upon observing the internal structure of the specimen, the addition of fibers leads to a relative reduction in the number of pores, particularly improving the presence of larger pores within the filler.
- (4) Reconstructing the fibers inside the filler, it is found that the orientation of BF in space is mostly close to the horizontal direction under the three doping conditions. With more fiber doping, the distribution characteristics become more significant.
- (5) The failure mode observed in the discrete element model of the filling, after parameter calibration, aligns closely with the laboratory test results. This correspondence highlights the feasibility of conducting discrete element simulations on the filling material. The same conclusion is drawn within the discrete element simulation, indicating that the distribution range of BF angles becomes more concentrated and trends toward the horizontal direction.

**Author Contributions:** Conceptualization, X.C. (Xi Chen) and H.J.; methodology, H.J.; software, X.C. (Xi Chen); validation, J.L.; formal analysis, J.L. and Y.Y.; investigation, X.C. (Xi Chen); resources, L.Y.; data curation, X.C. (Xinming Chen) and L.Y.; writing—original draft preparation, H.J.; writing—review and editing, J.L.; visualization, W.Z. and T.Y. All authors have read and agreed to the published version of the manuscript.

**Funding:** This research was funded by the National Natural Science Foundation of China, grant numbers 52374121, 51834001, and 52104129; the China Postdoctoral Science Foundation, grant number 2022T150195; the Key Science and the Technology Program of Henan Province: 222102220019.

**Data Availability Statement:** Data are contained within the article.

**Conflicts of Interest:** The authors declare no conflict of interest.

## References

1. Lyu, X.; Yang, K.; Fang, J. Utilization of resources in abandoned coal mines for carbon neutrality. *Sci. Total Environ.* **2022**, *822*, 153646. [[CrossRef](#)]
2. Wang, G.; Xu, Y.; Ren, H. Intelligent and ecological coal mining as well as clean utilization technology in China: Review and prospects. *Int. J. Min. Sci. Technol.* **2019**, *29*, 161–169. [[CrossRef](#)]
3. Cacciuttolo, C.; Atencio, E. Past, Present, and Future of Copper Mine Tailings Governance in Chile (1905–2022): A Review in One of the Leading Mining Countries in the World. *Int. J. Environ. Res. Public Health* **2022**, *19*, 13060. [[CrossRef](#)] [[PubMed](#)]
4. Geng, Y.; Peng, C.; Wang, Z.; Huang, S.; Zhou, P.; Li, D. Insights into the spatiotemporal differences in tailings seepage pollution by assessing the diversity and metabolic functions of the soil microbial community. *Environ. Pollut.* **2022**, *306*, 119408. [[CrossRef](#)]
5. Koppe, J.C. Lessons Learned from the Two Major Tailings Dam Accidents in Brazil. *Mine Water Environ.* **2021**, *40*, 166–173. [[CrossRef](#)]
6. Rose, R.; Mugi, S.; Saleh, J. Accident investigation and lessons not learned: AcciMap analysis of successive tailings dam collapses in Brazil. *Reliab. Eng. Syst. Saf.* **2023**, *236*, 109308. [[CrossRef](#)]
7. Sun, W.; Wu, D.; Liu, H.; Qu, C. Thermal, mechanical and ultrasonic properties of cemented tailings backfill subjected to microwave radiation. *Constr. Build. Mater.* **2021**, *313*, 125535. [[CrossRef](#)]
8. Xiu, Z.; Wang, S.; Ji, Y.; Wang, F.; Ren, F.; Nguyen, V. Loading rate effect on the uniaxial compressive strength (UCS) behavior of cemented paste backfill (CPB). *Constr. Build. Mater.* **2021**, *271*, 121526. [[CrossRef](#)]
9. Zhao, K.; Yu, X.; Zhu, S.; Zhou, Y.; Wang, Q.; Wang, J. Acoustic emission investigation of cemented paste backfill prepared with tantalum-niobium tailings. *Constr. Build. Mater.* **2020**, *237*, 117523. [[CrossRef](#)]
10. Jiang, G.; Wu, A.; Wang, Y.; Wang, Y.; Li, J. Determination of utilization strategies for hemihydrate phosphogypsum in cemented paste backfill: Used as cementitious material or aggregate. *J. Environ. Manag.* **2022**, *308*, 114687. [[CrossRef](#)]
11. Wang, B.; Xiong, T.; Gao, L.; Chai, Y.; Cui, X.; Ding, W. Effects of tailings gradation on rheological properties of filling slurry. *Adv. Civ. Eng.* **2019**, *2019*, 6873840. [[CrossRef](#)]
12. Li, D.; Fan, Y.; Dong, X.; Ma, X.; Liu, P. Mechanical Properties and Hydration Mechanism of Coal Flotation Tailing Cemented Filling Materials. *Minerals* **2023**, *13*, 389. [[CrossRef](#)]
13. Yang, L.; Li, J.; Jiao, H.; Wu, A.; Yin, S. Research on the Homogenization Evaluation of Cemented Paste Backfill in the Preparation Process Based on Image Texture Features. *Minerals* **2022**, *12*, 1622. [[CrossRef](#)]
14. Xie, H.; Gao, M.; Zhang, R.; Peng, G.; Wang, W.; Li, A. Study on the mechanical properties and mechanical response of coal mining at 1000 m or deeper. *Rock Mech. Rock Eng.* **2019**, *52*, 1475–1490. [[CrossRef](#)]
15. Han, B.; Sun, W.; Yu, S.; Liu, C.; Yao, S.; Wu, J. Performance comparison between neutralization tailings and flotation tailings used for backfill mix and mechanism analysis. *Adv. Mater. Sci. Eng.* **2016**, *2016*, 1087269. [[CrossRef](#)]
16. Lu, H.; Qi, C.; Chen, Q.; Gan, D.; Xue, Z.; Hu, Y. A new procedure for recycling waste tailings as cemented paste backfill to underground stopes and open pits. *J. Clean. Prod.* **2018**, *188*, 601–612. [[CrossRef](#)]
17. Huang, C.; He, W.; Lu, B.; Wang, M.; Li, S.; Xiao, C. Study on Acoustic Emission and Coda Wave Characteristics of Layered Cemented Tailings Backfill under Uniaxial Compression. *Minerals* **2022**, *12*, 896. [[CrossRef](#)]
18. Cavusoglu, I.; Yilmaz, E.; Yilmaz, A.O. Sodium silicate effect on setting properties, strength behavior and microstructure of cemented coal fly ash backfill. *Powder Technol.* **2021**, *384*, 17–28. [[CrossRef](#)]
19. Jiao, H.; Zhang, W.; Yang, Y.; Chen, X.; Yang, L.; Shen, H.; Rong, Y.; Zhang, H. Static mechanical characteristics and meso-damage evolution characteristics of layered backfill under the condition of inclined interface. *Constr. Build. Mater.* **2023**, *366*, 130113. [[CrossRef](#)]
20. Chen, X.; Zhang, J.; Jiao, H.; Hu, K.; Wan, L.; Ruan, Z.; Yang, L. Mechanism of rake frame shear drainage during gravity dewatering of ultrafine unclassified tailings for paste preparation. *Minerals* **2022**, *12*, 240. [[CrossRef](#)]
21. Zheng, B.; Zhang, D.; Liu, W.; Yang, Y.; Yang, H. Use of Basalt Fiber-Reinforced Tailings for Improving the Stability of Tailings Dam. *Materials* **2019**, *12*, 1306. [[CrossRef](#)] [[PubMed](#)]
22. Jiang, P.; Lv, S.; Wang, Y.; Li, N.; Wang, W. Investigation on Direct Shear and Energy Dissipation Characteristics of Iron Tailings Powder Reinforced by Polypropylene Fiber. *Appl. Sci.* **2019**, *9*, 5098. [[CrossRef](#)]

23. Zheng, W.; Wang, S.; Qu, Y.; Liu, K.; Jia, L. Research on Mechanical and Carbonization Properties of Hybrid Fiber Iron Tailings Concrete Based on Deep Learning. *Comput. Intell. Neurosci.* **2022**, *2022*, 3475679. [[CrossRef](#)] [[PubMed](#)]
24. Yan, R.; Liu, J.; Yin, S.; Zou, L.; Kou, Y.; Zhang, P. Effect of polypropylene fiber and coarse aggregate on the ductility and fluidity of cemented tailings backfill. *J. Cent. South Univ.* **2022**, *29*, 515–527. [[CrossRef](#)]
25. Zheng, W.; Wang, S.; Quan, X.; Qu, Y.; Mo, Z.; Lin, C. Carbonation Resistance and Pore Structure of Mixed-Fiber-Reinforced Concrete Containing Fine Aggregates of Iron Ore Tailings. *Materials* **2022**, *15*, 8992. [[CrossRef](#)] [[PubMed](#)]
26. Jiang, P.; Chen, L.; Li, N.; Qian, J.; Wang, W. Study on the mechanical properties of fiber-modified iron tailings stabilized by lime and fly ash based on energy analysis. *Case Stud. Constr. Mater.* **2022**, *17*, e01638. [[CrossRef](#)]
27. Yang, L.; Jia, H.; Jiao, H.; Dong, M.; Yang, T. The Mechanism of Viscosity-Enhancing Admixture in Backfill Slurry and the Evolution of Its Rheological Properties. *Minerals* **2023**, *13*, 1045. [[CrossRef](#)]
28. Yang, J.; Zhao, K.; Yu, X.; Yan, Y.; He, Z.; Zhou, Y.; Lai, Y. Fracture evolution of fiber-reinforced backfill based on acoustic emission fractal dimension and b-value. *Cem. Concr. Compos.* **2022**, *134*, 104739. [[CrossRef](#)]
29. Xue, G.; Yilmaz, E.; Feng, G.; Cao, S. Analysis of tensile mechanical characteristics of fibre reinforced backfill through splitting tensile and three-point bending tests. *Int. J. Min. Reclam. Environ.* **2022**, *36*, 218–234. [[CrossRef](#)]
30. Jiao, H.; Wu, Y.; Wang, H.; Chen, X.; Li, Z.; Wang, Y.; Zhang, B.; Liu, J. Micro-scale mechanism of sealed water seepage and thickening from tailings bed in rake shearing thickener. *Miner. Eng.* **2021**, *17*, 107043. [[CrossRef](#)]
31. Xue, G.; Yilmaz, E. Strength, acoustic, and fractal behavior of fiber reinforced cemented tailings backfill subjected to triaxial compression loads. *Constr. Build. Mater.* **2022**, *338*, 127667. [[CrossRef](#)]
32. Xu, W.; Li, Q.; Zhang, Y. Influence of temperature on compressive strength, microstructure properties and failure pattern of fiber-reinforced cemented tailings backfill. *Constr. Build. Mater.* **2019**, *222*, 776–785. [[CrossRef](#)]
33. Yang, L.; Li, J.; Liu, H.; Jiao, H.; Yin, S.; Chen, X.; Yu, Y. Systematic review of mixing technology for recycling waste tailings as cemented paste backfill in mines in China. *Int. J. Miner. Metall. Mater.* **2023**, *30*, 1–14. [[CrossRef](#)]
34. Gao, B.; Cao, S.; Yilmaz, E. Effect of Content and Length of Polypropylene Fibers on Strength and Microstructure of Cementitious Tailings-Waste Rock Fill. *Minerals* **2023**, *13*, 142. [[CrossRef](#)]
35. Jiang, P.; Chen, Y.; Li, N.; Wang, W. Cumulative Deformation and Damage Evolution of Fiber Cement-Modified Iron Tailings under Cyclic Load. *Int. J. Geomech.* **2023**, *23*. [[CrossRef](#)]
36. Jiang, F.; Tan, B.; Wang, Z.; Liu, Y.; Hao, Y.; Zhang, C.; Wu, H.; Hong, C. Preparation and related properties of geopolymer solidified uranium tailings bodies with various fibers and fiber content. *Environ. Sci. Pollut. Res.* **2022**, *29*, 20603–20616. [[CrossRef](#)]
37. Chen, X.; Shi, X.; Zhou, J.; Yu, Z.; Huang, P. Determination of mechanical, flowability, and microstructural properties of cemented tailings backfill containing rice straw. *Constr. Build. Mater.* **2020**, *246*, 118520. [[CrossRef](#)]
38. Zhao, K.; Zhao, K.; Yan, Y.; Yang, J.; Wu, J.; Lai, Y.; Liu, L.; Zeng, X. Influence of different fibers on compressive toughness and damage of early age cemented tailings backfill. *Environ. Sci. Pollut. Res.* **2023**, *30*, 37449–37461. [[CrossRef](#)]
39. Sotomayor, J.; Alelvan, G.; Casagrande, M. Influence of Polypropylene Fiber-Reinforcement on the Mechanical Behavior of Gold Ore Tailings through Direct Shear Tests. *J. Mater. Civ. Eng.* **2021**, *33*. [[CrossRef](#)]
40. Zhang, Z.; Wang, W.; Zhao, B. Numerical Study on the Vibratory Compaction Mechanism of the Sand-Gabion Backfills in Underground Coal Mines. *Minerals* **2022**, *12*, 1428. [[CrossRef](#)]
41. Xue, X.; Gu, Y.; Zhang, X.; Wu, S.; Sun, P.; Cui, J.; Wang, X. Mechanical behavior and microscopic mechanism of fiber reinforced coarse aggregate cemented backfill. *Constr. Build. Mater.* **2023**, *366*, 130093. [[CrossRef](#)]
42. Chen, X.; Shi, X.; Zhou, J.; Yu, Z. Influence of polypropylene fiber reinforcement on tensile behavior and failure mode of tailings cemented paste backfill. *IEEE Access* **2019**, *7*, 69015–69026. [[CrossRef](#)]
43. Cao, S.; Yilmaz, E.; Yin, Z.; Xue, G.; Song, W.; Sun, L. CT scanning of internal crack mechanism and strength behavior of cement-fiber-tailings matrix composites. *Cem. Concr. Compos.* **2021**, *116*, 103865. [[CrossRef](#)]
44. Wang, D.; Zeng, F.; Wei, J.; Zhang, H.; Wu, Y.; Wei, Q. Quantitative analysis of fracture dynamic evolution in coal subjected to uniaxial and triaxial compression loads based on industrial CT and fractal theory. *J. Pet. Sci. Eng.* **2021**, *196*, 108051. [[CrossRef](#)]
45. Jiao, H.; Yang, W.; Ruan, Z.; Yu, J.; Liu, J.; Yang, Y. The micro-scale mechanism of tailings thickening processing from metal mines. *Int. J. Miner. Metall. Mater.* **2022**, *30*, 1538–1547. [[CrossRef](#)]
46. Li, J.; Cao, S.; Yilmaz, E. Characterization of macro mechanical properties and microstructures of cement-based composites prepared from fly ash, gypsum and steel slag. *Minerals* **2022**, *12*, 6. [[CrossRef](#)]
47. Alberti, M.G.; Enfedaque, A.; Gálvez, J.C. Fracture mechanics of polyolefin fibre reinforced concrete: Study of the influence of the concrete properties, casting procedures, the fibre length and specimen size. *Eng. Fract. Mech.* **2016**, *154*, 225–244. [[CrossRef](#)]
48. Zhu, C.; Zhou, N.; Guo, Y.; Li, M.; Cheng, Q. Effect of doped glass fibers on tensile and shear strengths and microstructure of the modified shotcrete material: An experimental study and a simplified 2D model. *Minerals* **2021**, *11*, 1053. [[CrossRef](#)]
49. Jiang, P.; Zhou, L.; Wang, Y.; Qian, B.; Wang, W.; Li, N.; Zhang, F. Freeze–Thaw Damage Model of Polypropylene Fiber Reinforced Cement Stabilized Waste Construction Slurry under Uniaxial Action. *Minerals* **2021**, *11*, 743. [[CrossRef](#)]
50. Yu, H.; Liu, H.; Hang, Y.; Liu, J.; Ma, S. Deformation and failure mechanism of weakly cemented mudstone under Tri-Axial compression: From laboratory tests to numerical simulation. *Minerals* **2022**, *12*, 153. [[CrossRef](#)]
51. Xu, X.; Wu, W.; Xu, W. Sulfate-dependent shear behavior of cementing fiber-reinforced tailings and rock. *Minerals* **2020**, *10*, 1032. [[CrossRef](#)]

52. Khan, M.; Cao, M.; Xie, C.; Ali, M. Efficiency of basalt fiber length and content on mechanical and microstructural properties of hybrid fiber concrete. *Fatigue Fract. Eng. Mater. Struct.* **2021**, *44*, 2135–2152. [[CrossRef](#)]
53. Wang, S.; Liu, Z.; Liu, Y.; Deng, N.; Yang, B.; Tan, L. Contribution of Triassic Tectonomagmatic Activity to the Mineralization of Liziyuan Orogenic Gold Deposits, West Qinling Orogenic Belt, China. *Minerals* **2023**, *13*, 130. [[CrossRef](#)]
54. Gao, T.; Sun, W.; Li, Z.; Fan, K.; Jiang, M.; Cheng, H. Study on shear characteristics and failure mechanism of inclined layered backfill in mining solid waste utilization. *Minerals* **2022**, *12*, 1540. [[CrossRef](#)]

**Disclaimer/Publisher's Note:** The statements, opinions and data contained in all publications are solely those of the individual author(s) and contributor(s) and not of MDPI and/or the editor(s). MDPI and/or the editor(s) disclaim responsibility for any injury to people or property resulting from any ideas, methods, instructions or products referred to in the content.